

Contents lists available at ScienceDirect

# Nuclear Inst. and Methods in Physics Research, A

journal homepage: www.elsevier.com/locate/nima



# Full Length Article

# New method for level-lifetime measurements with thick scintillators





- <sup>a</sup> Department of Physics and Astronomy, Mississippi State University, Mississippi State, MS 39762, USA
- b Los Alamos National Laboratory, Los Alamos, NM 87545, USA
- <sup>c</sup> Facility for Rare Isotope Beams, Michigan State University, East Lansing, MI 48824, USA
- <sup>d</sup> Department of Chemistry, Michigan State University, East Lansing, MI 48824, USA
- e GSI Helmholtzzentrum für Schwerionenforschung, Planckstr. 1, 64291 Darmstadt, Germany
- <sup>f</sup> Department of Physics, Al al-Bayt University, Mafraq 25113, Jordan
- g Department of Physics and Astronomy, University of Tennessee, Knoxville, TN 37996, USA
- h Department of Physics and Astronomy, University of North Carolina at Chapel Hill, Chapel Hill, NC 27599, USA
- <sup>i</sup> Triangle Universities Nuclear Laboratory, Duke University, Durham, NC 27708, USA
- <sup>j</sup> Physics Division, Argonne National Laboratory, Argonne, IL 60439, USA
- k DEVCOM/Army Research Laboratory, Adelphi, MD 20783, USA
- Department of Physics and The Joint Institute for Nuclear Astrophysics, University of Notre Dame, Notre Dame, IN 46556-5670, USA
- m Physics Division, Oak Ridge National Laboratory, Oak Ridge, TN 37830, USA
- <sup>n</sup> Department of Chemistry and Biochemistry, University of Maryland, College Park, MD 20742, USA
- o Idaho National Laboratory, Idaho Falls, ID 83415, USA
- p National Superconducting Cyclotron Laboratory, Michigan State University, East Lansing, MI 48824, USA
- <sup>q</sup> Department of Physics and Astronomy, Michigan State University, East Lansing, MI 48824, USA
- <sup>r</sup> Dipartimento di Fisica e Astronomia, Università degli Studi di Padova, I-35131 Padova, Italy
- <sup>s</sup> Department of Nuclear Engineering, University of California Berkeley, Berkeley, CA 94720, USA
- <sup>t</sup> National Nuclear Data Center, Brookhaven National Laboratory, Upton, NY 11973, USA

#### ARTICLE INFO

# Keywords: Fast timing Rare isotope studies Ion implantation Beta decay Scintillator detectors Gamma-ray spectroscopy

#### ABSTRACT

Level lifetimes provide key insight into the structure of atomic nuclei and serve as stringent tests of theoretical descriptions. Though several methods for determining level lifetimes exist for both reaction measurements and decay studies, here the focus is on techniques involving the direct measurement of time differences between population and subsequent depopulation of excited states. The techniques presented herein are broadly applicable across multiple timing ranges, but the approach is specifically described for the  $\beta\gamma$  timing method. A multi-step, amplitude-dependent time walk correction and timing resolution corrections were employed to address the data analysis complications that arise from using thick scintillators for electron detection. Subsequently, a new Monte Carlo method utilizing measured detector responses obtained from the data, coupled with chi-square minimization, is presented for extracting excited state lifetimes  $\gtrsim 100$  picoseconds. The framework of this Monte Carlo method is developed for the decay of a state in 68 Zn with a known 1.6 ps half life, which is considered prompt given the detection sensitivity of the technique, and then benchmarked using two other excited states in neutron-rich Ni isotopes with 120(34) ps and 1.05(3) ns half lives. Using this new method which takes into account the thick scintillator used, these same half lives were measured to be 135(10) ps and 1.04(24) ns, respectively. The overall good agreement demonstrates the validity of the technique.

# 1. Introduction

Within the atomic nucleus, there are typically many excited states above the ground state, which can be associated with unique configurations of the constituent nucleons. Due to the complex nature of

E-mail addresses: bpc135@msstate.edu (B.P. Crider), prokop@nscl.msu.edu (C.J. Prokop), liddick@nscl.msu.edu (S.N. Liddick).

Deceased.

https://doi.org/10.1016/j.nima.2023.168525

Received 24 April 2023; Received in revised form 30 June 2023; Accepted 2 July 2023 Available online 7 July 2023

0168-9002/© 2023 Elsevier B.V. All rights reserved.

<sup>\*</sup> Corresponding author.

the nuclear force, and its interactions within a many-body quantum system, the location and spacing of these excited states constantly evolve across the nuclear chart. These states, observed experimentally through spectroscopy, often correspond to complex wavefunctions.

In many instances, theoretical models are capable of reproducing the energy of excited states throughout the low-to-medium mass nuclei. However, a much more stringent test of nuclear theory is the reproduction of the strengths of transitions connecting various levels within the nucleus. The so-called transition strength is a measure of the probability of an excited state decaying to some other level, which is mediated by one or more multipole terms of the electromagnetic field. As such, it serves as a unique fingerprint of the underlying configurations of the states involved. The transition strength is inversely proportional to the partial half life of the transition. Thus, knowledge of the decay half-lives is required to deduce this quantity for many types of measurements, such as ones utilizing  $\beta$  decay to populate excited states in a daughter nucleus.

The need for transition strength information is ever increasing, as the prevalence of competing and coexisting nuclear shapes has transitioned from being an exotic rarity to becoming an ubiquity in nuclei at or near closed shells. The presence of these so-called shape coexisting structures originates from effective nucleon-nucleon interactions that can rearrange the single-particle states, thereby modifying the energy gaps between the levels or eliminating them altogether [1,2]. With a reduction of the energy gap, excitations of nucleons across this gap into higher-lying single-particle states become more probable and the resulting proton-neutron interactions can stabilize the system by substantially increasing the binding energy. If these excited configurations are associated with different shapes than those for the lower-lying configurations, the different structures can coexist at similar energies and lead to potential isomeric transitions between them. Many of these types of isomers have lifetimes that can be measured via the techniques presented herein with implantation scintillators. The data in turn allow for the possibility of determining the transition strengths between the shape isomers and result in an enhanced understanding of nuclear structure that can be instrumental in improving theoretical calculations.

Over many years, a variety of experimental techniques have been developed to measure lifetimes of excited nuclear states across several orders of magnitude (see, for example, Refs. [3-5]). For sub-picosecond half lives, the Doppler-shift Attenuation Method (DSAM) [6] is primarily used to deduce the half life of the decaying state by measuring a shift in the energy of an emitted  $\gamma$  ray from an excited state in the recoiling parent nucleus at a variety of forward and backward angles. For picosecond to nanosecond half-lives, the Recoil Distance Method (RDM) [7] and ensuing variants of that technique, can be applied. A few examples of these variations using different experimental setups and analysis techniques include: the Recoil Distance Doppler-Shift (RDDS) [8,9] method; Delayed Coincidence Counting (DCC) [10,11] using  $\beta\gamma$ ,  $\beta\gamma\gamma$ , and  $\gamma\gamma$  coincidences with fast-timing detectors such as plastic scintillators, LaBr<sub>3</sub>(Ce), CeBr<sub>3</sub>, and BaF<sub>2</sub> detectors; and the Time Interval Distribution Analysis Method [12,13]. As a particular example for cases where the excited state lifetime exceeds ~ 10 ps, techniques such as Delayed Coincidence Counting which involve measuring the time difference between the population and subsequent depopulation of the excited state become viable. The half life is extracted from a shift in the centroid of the delayed time-difference distribution compared to one corresponding to a prompt deexcitation or from fitting the timedifference distribution with a convolution of the detector response and a decaying exponential [10,14].

In this manuscript, attention is given to these time difference methods, specifically  $\beta\gamma$  and  $\beta\gamma\gamma$  techniques, applicable to lifetimes  $\gtrsim 100$  ps. The techniques described herein are aimed at addressing complications that arise from using a thick implantation scintillator to perform fast-timing measurements. These thick scintillators can be a necessary complication when implanting rare isotope beams into a

fast scintillator with low Z. While specifically tailored to extracting results with a thick scintillator, the techniques are broadly applicable. Section 2 describes in more detail the  $\beta\gamma$  and  $\beta\gamma\gamma$  methods along with some experimental considerations for applying them. A description of the experiment from which the data used for this work originates is presented in Section 3. The complications to  $\beta\gamma$  timing that arise when utilizing thick scintillators for  $\beta$ -decay electron detection are presented in Section 4. Section 5 presents a new method particularly designed to overcome the limitations encountered when using a thick scintillator. Finally, within the same section, the new technique is validated using data for two excited states in  $^{69}$ Co and  $^{70}$ Co with known lifetimes from recent  $\beta$ -decay spectroscopy experiments, performed at the National Superconducting Cyclotron Laboratory (NSCL). Section 6 provides a brief conclusion and summarizes the method and its achievements.

## 2. $\beta \gamma$ and $\beta \gamma \gamma$ lifetime methods

The  $\beta\gamma$  and  $\beta\gamma\gamma$  lifetime measurement techniques rely on obtaining the relative time difference between the population and depopulation of isomeric states. In the  $\beta\gamma$  variant, the isomer is populated through  $\beta$  decay, either directly or indirectly, and some time later a  $\gamma$  ray is emitted. If the  $\beta$  decay populates this state indirectly, and the ensuing cascade propagates through a higher-lying level with a measurable lifetime (via DCC), the results will be skewed.

The  $\beta\gamma\gamma$  method has the same basic principle, but the isomer of interest is always populated indirectly by  $\beta$  decay. The timing information can be extracted from any pair of  $\gamma$  rays where one populates and the other depopulates the isomeric level of interest, and the detection of the  $\beta$ -decay electron serves to reduce the random coincidence events that otherwise contaminate the  $\gamma\gamma$  spectrum. Alternatively, the timing information can be extracted from the  $\beta$ --decay electron and one of the γ rays depopulating the isomeric level of interest, where the second  $\gamma$  ray is used to reduce the random coincidence events. Though this method provides very clean spectra, one obvious disadvantage is the reduction in statistics incurred by requiring the detection of the second  $\gamma$  ray. Thus, the  $\beta\gamma\gamma$  method is often not applicable when the  $\gamma$ -ray transition intensity, either in or out of the state of interest, is small. Furthermore, when measuring exotic nuclei far from stability where production rates are generally low, there is often not sufficient statistics for this technique regardless of branching ratios. The <sup>69</sup>Ni and <sup>70</sup>Ni data used for the present study fall in such a category where statistics limitations require the  $\beta \gamma$  technique be employed.

Typically in  $\beta\gamma$  timing experiments, thin plastic scintillators are employed to detect the  $\beta^-$  decay electron and larger-volume inorganic scintillators, such as the LaBr<sub>3</sub>(Ce) detectors used in the present study, detect delayed  $\gamma$  rays. These detectors are chosen because of their excellent intrinsic time resolution and, in the case of LaBr<sub>3</sub>(Ce) detectors, good energy resolution. Instrumentation of these detectors requires acquisition electronics with electronic time resolution suitable to take advantage of the capabilities of the detectors. Previous publications have detailed the Digital Data Acquisition System (DDAS) [15] used in this study, along with methods to simultaneously obtain high-resolution time and energy extraction from fast scintillator detectors [16]. The work of Ref. [16] demonstrated time resolutions on the order of a few hundred picoseconds full width at half maximum (FWHM) for DDAS when instrumenting fast scintillators.

# 3. Experimental description

The experiment was performed at the National Superconducting Cyclotron Laboratory (NSCL) and used the coupled cyclotron facility to accelerate a primary beam of  $^{76}$ Ge to 140 MeV/A which impinged onto 282 mg/cm $^2$   $^9$ Be target. Fragments of interest were selected by their momentum-to-charge ratio (p/q) using the A1900 fragment separator [17] and delivered to the experimental end station.

All ions underwent event-by-event identification using the energy loss in a Si PIN detector located upstream from the implantation detector and the time of flight between the fragment separator and the same Si PIN counter. The former is sensitive to the atomic number of the ion while the latter is proportional to the momentum to charge ratio of the incoming ion. This technique provides unambiguous identification of all beam species incident on the experimental end station.

The experimental end station was comprised of a  $52 \times 52 \times 10 \text{ mm}^3$  ELJEN EJ-204 segmented plastic scintillator. The internal grid of light guides, oriented along the beam axis, defined a grid of 256 discrete pixels, each with a size of  $3.25 \times 3.25 \text{ mm}^2$ . The segmented scintillator was read out using a Hamamatsu H8500C-03 Position Sensitive Photo-Multiplier Tube (PSPMT) with 64 discrete pixels. The intrinsic 256-pixel resolution afforded by the scintillator was obtained using a "center-of-gravity" algorithm described in Ref. [18].

An array of ten Saint Gobain BrilLanCe  $380^{\$}$   $38 \text{ mm} \times 38 \text{ mm}$  right-cylindrical LaBr $_3$ (Ce) detectors instrumented with Hamamatsu R6231 PMTs surrounded the segmented plastic scintillator. The segmented plastic scintillator and LaBr $_3$ (Ce) array were, in turn, surround by 16 detectors of the Segmented Germanium Array (SeGA) [19], arranged into two concentric rings.

All detectors were instrumented using DDAS [15,16]. A new DDAS module with 12-bit, 500 Mega Samples Per Second (MSPS) digitizers was employed for the dynode signal from the PSPMT and all LaBr $_3$ (Ce) scintillator to maximize the time-resolving capabilities of the system. The PSPMT anodes and all other detectors were read out by 14-bit, 250 MSPS digitizers.

In this experiment, ions of interest were implanted two to three millimeters deep into the plastic scintillator. The x/y position and arrival time of each ion was recorded. Some time later, the implanted ion  $\beta$  decayed and the energy, position, and time of the electron, as well as the energy and time of any detected  $\gamma$  rays, were all recorded. Decays were then correlated to a specific ion using the spacial and temporal information. In this way, the segmentation of the plastic scintillator is crucial to obtain precise position information. The 10 mm thickness of the scintillator material serves to increase the electron detection efficiency and provides a large amount of material for the fast beam to deposit energy and come to rest, offering a wide range of applications even for experiments with much lighter nuclei.

# 4. Considerations for timing with thick scintillators

The 10 mm thickness of the particular scintillator used in the experiment described in Section 3 complicates the extraction of the  $\beta\gamma$  timing information and requires considerations beyond those typically necessary for thin scintillators. In a thick scintillator, the detector response is highly coupled to the energy deposited. This coupling manifests itself as changes to both the centroid and time resolution as a function of energy and leads to two important consequences. First, the correction for the amplitude-dependent time walk must be performed for not only the LaBr<sub>3</sub>(Ce) detectors, but also for the segmented plastic scintillator in a multi-step process. A technique for doing this is presented in Section 5.1. Second, the time difference spectrum between the discreteenergy  $\gamma$  ray detected in the LaBr<sub>3</sub>(Ce) and the  $\beta$ -decay electron in the plastic scintillator cannot be treated simply as a single Gaussian detector response convoluted with an exponential decay. This is due to widely varying plastic scintillator responses across the range of the continuous electron energy distribution obtained from  $\beta$  decay. The technique described throughout the remainder of the paper was developed to address this issue specifically.

Other effects that must be accounted for in this particular experiment, where the decaying ions of interest have been implanted into the scintillator, are the difference in the interaction point distributions between calibration and experiment as well as the energy profile of emitted radiation. Gamma rays emitted from a source external to the detector will have a different interaction depth and energy profiles than

the electrons emanating from decays of the implanted ions. In particular, the dependence of the scintillator time resolution on the interaction depth has been explored by the medical imaging community (see, e.g., Refs. [20,21], and those found within) and a technique has been adapted to address these considerations for the current application, which is presented in Section 5.2.

#### 5. New method for $\beta \gamma$ timing with thick scintillators

In this section, the entire process is outlined for obtaining the  $\beta\gamma$  timing information for the experimental array described in Section 3, which utilizes a thick segmented plastic implantation scintillator to detect electrons emitted in  $\beta$  decay. The techniques to handle the amplitude-dependent time walk are presented in Section 5.1 and the characterization and subsequent development of the combination of depth of interaction (DOI) and differing emitted radiation energy distribution corrections are provided in Section 5.2. Finally, the new Monte Carlo method developed to extract excited state lifetimes using detector responses obtained from a  $^{60}$ Co source is presented in Section 5.3. This section concludes by benchmarking the new method with two excited states with well-known lifetimes.

#### 5.1. Walk corrections

The first step in the analysis of  $\beta\gamma$  or  $\beta\gamma\gamma$  timing experiments involves correcting the time response of each detector for the pulse-amplitude dependent time walk. Though usage of a digital Constant Fraction Discriminator (CFD) [22] minimizes the time walk, it still persists at the hundreds of picoseconds level across the dynamic range and, hence, must be removed.

The walk correction technique involves the use of  $^{60}$ Co source, which decays predominately (99.9% branch) to the 2505.7-keV state in  $^{60}$ Ni [23]. This decay yields a cascade of two  $\gamma$  rays in coincidence with energies of 1173.2 and 1332.5 keV, where the 1332.5-keV level in  $^{60}$ Ni has a half life of 0.9 ps [24]. This short half-life is below the sensitivity of the  $\beta\gamma$  technique, as implemented in this experimental setup, thus the coincidence events are considered to be prompt.

The process proceeds by collecting data with the full experimental array, and recording the energies and times for all coincident  $\gamma$  rays detected in the segmented plastic scintillator and the LaBr<sub>3</sub>(Ce) detectors. The time-difference between the LaBr<sub>3</sub>(Ce) detectors and the plastic scintillator PSPMT dynode is then calculated for each event and stored with the LaBr<sub>3</sub>(Ce) and plastic scintillator energy in ten, three-dimensional histograms; one for each LaBr<sub>3</sub>(Ce) detector.

A preliminary, coarse time-offset correction is applied to the time differences uniformly across the LaBr<sub>3</sub>(Ce) and plastic scintillator PSPMT dynode dynamic ranges to account for differences in cable lengths and digitizer synchronization for each LaBr<sub>3</sub>(Ce) detector with the ultimate goal to facilitate summing of statistics, when applicable. In this step, an artificial time-difference offset of 1000 ns is introduced to avoid negative time differences.

To determine and calibrate the plastic scintillator time response, a two-dimensional projection of each three-dimensional histogram described above is taken over both the 1173.2- and 1332.5-keV  $\gamma$  photopeak energy regions in the LaBr $_3$ (Ce) detectors. This provides a region with low time walk variability, high statistics, and good time resolution for investigating the plastic scintillator (dynode) time walk. The sum of all ten, two-dimensional histograms, shown in Fig. 1(a), presents the dynode amplitude vs. time difference. For each dynode amplitude bin in Fig. 1(a), the centroid of the projection onto the time-difference axis, obtained from a Gaussian fit, is displayed in Fig. 1(b). These centroid values are then fit with a high-order (9th order) polynomial, shown as a red line in Fig. 1(b), to extract the walk correction as a function of the dynode signal amplitude.

The result of the dynode walk correction is illustrated in Figs. 1c and 1d. The corrected, two-dimensional dynode amplitude vs. time-difference spectrum is shown in Fig. 1c while Fig. 1d displays the

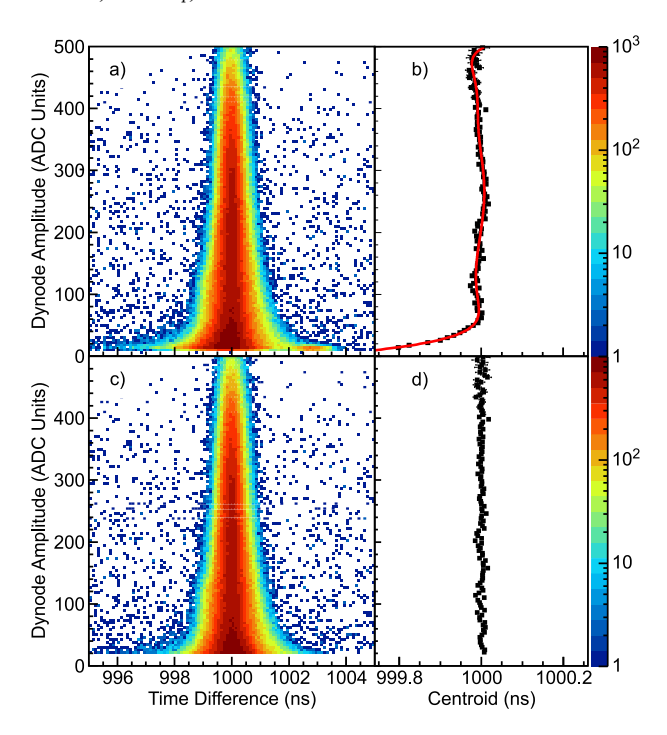


Fig. 1. (a) Two-dimensional histogram of the dynode signal amplitude plotted against the LaBr $_3$ (Ce) - PSMPT dynode time difference summed for all LaBr $_3$ (Ce) detectors gated on either the 1173.2- or 1332.5-keV  $\gamma$  photopeak in the respective LaBr $_3$ (Ce) detector. (b) Plot of centroid position, extracted from fitting the projection of each bin in (a) onto the time-difference axis. A high order polynomial, shown in red, was used for interpolation between the data to extract the time walk as a function of dynode signal amplitude. Panels (c) and (d) show the same histograms after application of this correction. Even after determination of the walk correction, a slightly higher threshold of 20 ADC units was applied in the final, walk-corrected histograms to ensure CFD timing, as opposed to leading-edge timing, was utilized. In panels (b) and (d), the time difference axis was zoomed in to better show the changes in centroid position.

dynode, walk-corrected, time-difference centroid values for each bin of Fig. 1(c). The walk correction is valid for dynode amplitude ranges of 20 to 500 ADC units, and the resulting centroid values are all within 10 ps of the 1000 ns offset across the entire dynode dynamic range.

With the walk correction for the dynode complete, the focus shifts to correcting the LaBr<sub>3</sub>(Ce) detector response. To obtain the time walk as a function of LaBr<sub>3</sub>(Ce) detector energy, each bin of the dynode walk-corrected two-dimensional dynode-signal amplitude vs. time difference histogram, see Fig. 2a for one of the ten LaBr<sub>3</sub>(Ce) detectors, is projected onto the time-difference axis and fit with a Gaussian. Specific regions corresponding to the Compton edges and backscatter peaks of both the 1173.2 and 1332.5 keV photopeaks have been removed from the spectrum shown in Fig. 2a due to anomalous behavior observed in the time response over these regions. Throughout the energy range of any detector in the array, the spectrum consists of an average of Compton scattering and photoelectric effects with both complete and incomplete light collection, which effectively washes out the differences in response to either photon interaction mechanism in the detector.

Most events where a coincidence exists between the plastic scintillator and one of the LaBr $_3$ (Ce) detectors are the result of detecting part or all of the energy from two individual  $\gamma$  rays. However, if a single  $\gamma$  ray Compton scatters outside of one of the detectors or Compton scatters at a very shallow depth in a detector, the possibility exists to detect the resulting electron in one detector and the scattered  $\gamma$  ray in another detector. These events appear to enhance the Compton edges and backscatter peaks. At the Compton edges of the 1173.2-

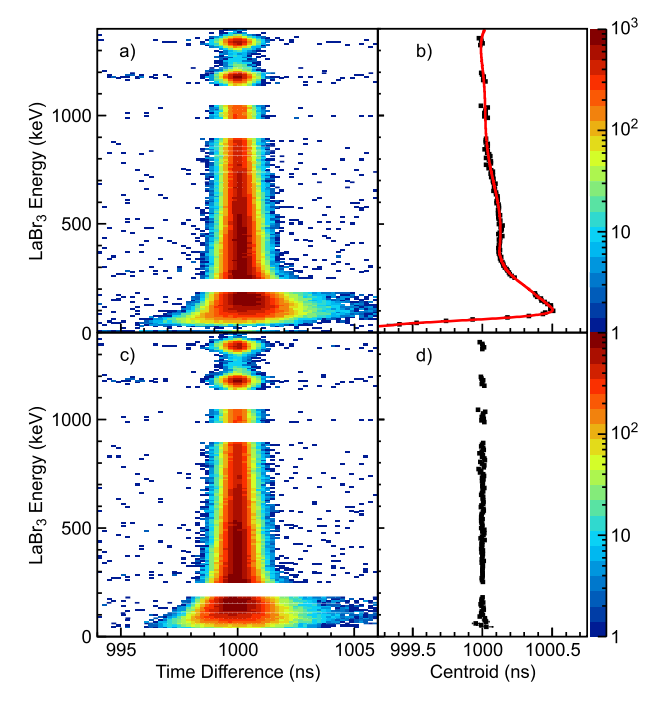


Fig. 2. (a) Two-dimensional histogram of the LaBr<sub>3</sub>(Ce) energy plotted against the LaBr<sub>3</sub>(Ce) - PSMPT dynode time difference for a single LaBr<sub>3</sub>(Ce) detector gated on dynode amplitudes between 20 and 500 ADC units. (b) Plot of centroid position for each LaBr<sub>3</sub>(Ce) energy bin, extracted from fitting the projection of each bin in (a) onto the time-difference axis. A high order polynomial, shown in red, was used extract the time walk as a function of LaBr<sub>3</sub>(Ce) energy. Panels (c) and (d) display the same histograms after application of this correction.

and 1332.5-keV  $\gamma$  rays in the LaBr<sub>3</sub>(Ce) detector, we detect the highenergy electron while some number of times the low-energy  $\gamma$  ray escapes into the plastic scintillator. At the backscatter peak in the LaBr<sub>3</sub>(Ce) detector, we observe a low-energy  $\gamma$  ray and the high-energy electron is detected in the plastic scintillator. In the former case, the centroid values are systematically low and, in the latter, they are systematically high. These discrete features at those specific energies are not representative of the time response of the detector but are an artifact of coincidence relationships between Compton scattering products of a single  $\gamma$  ray detected in coincidence in both detectors and probing the timing response difference between  $\gamma$  rays and electrons in the two types of scintillator detectors.

Fig. 2b presents the centroid position extracted from the fit of the projection of each LaBr<sub>3</sub>(Ce) detector energy bin in Fig. 2a. These centroid values are then fit with a high-order polynomial (red line in Fig. 2b) to extract the walk correction as a function of LaBr<sub>3</sub>(Ce) energy.

The result of the LaBr $_3$ (Ce) walk correction can be judged from Figs. 2c and 2d. Fig. 2c displays the corrected two-dimensional LaBr $_3$ (Ce) energy vs. dynode and LaBr $_3$ (Ce) walk-corrected time difference spectrum, while Fig. 2d corresponds to the dynode and LaBr $_3$ (Ce) walk-corrected time-difference centroid values for each bin of Fig. 2c. The walk correction is valid for LaBr $_3$ (Ce) energy ranges of 30 to 1400 keV and the resulting centroid values are all within 50 ps of the 1000 ns offset across the entire dynode dynamic range.

# 5.2. Accounting for differences between source and experimental data

The walk-calibration method presented in the previous subsection is sensitive to the coupling of the plastic scintillator dynode and  $LaBr_3(Ce)$  responses. The dynode amplitude distribution coincident with the 1173.2- and 1332.5-keV photopeaks in the  $LaBr_3(Ce)$  detectors

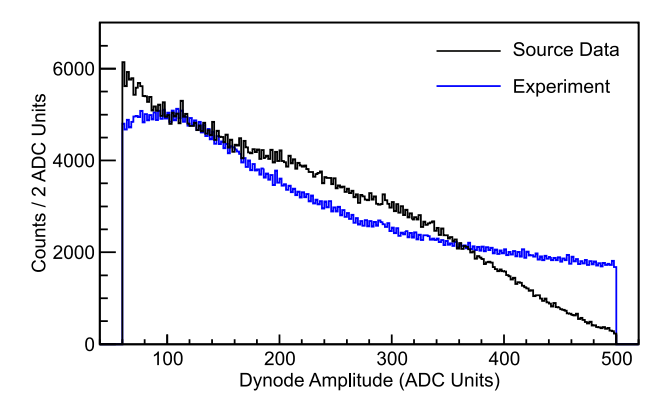


Fig. 3. Plot of the dynode amplitude distributions observed in coincidence with the 1173.2- and 1332.5-keV photopeaks in the  $LaBr_3(Ce)$  detectors from the source data (black) and the dynode amplitude distributions, normalized to the same integrated counts, observed in coincidence with the  $LaBr_3(Ce)$  detectors from 30 to 1400 keV during the experiment (blue).

from the source data is not representative of the distribution coincident with the  ${\rm LaBr_3(Ce)}$  detectors during the experiment. The nature of the different dynode amplitude distributions in source and experimental data arises from effects due to differences in emitted radiation energy profiles. Moreover, the energy distribution of emitted radiation, as well as depth of interaction (DOI) effects, will be distinct for each experiments and source. The differences in emitted radiation energy distributions and DOI effects result in pulse-height dependencies. While considering differing emitted radiation energy distribution and DOI effects independently is not possible in the technique being described in this manuscript, we can treat their combined effects on time walk and timing resolution separately. We begin with treating the effect on time-walk corrections.

Fig. 3 illustrates the dynode amplitude distribution from source data in black and from the experimental data in blue, where the experimental dynode amplitude distribution was observed from  $\beta^-$  decay electrons in the region of nuclei around <sup>68</sup>Ni and in coincidence with detected  $\gamma$  rays from 30 to 1400 keV in the LaBr<sub>3</sub>(Ce) detectors, and has been normalized to the integrated counts found in the source data. For the analyses presented here, the dynode signal amplitude is restricted to be >60 and still <500 ADC Units in order to prevent the low amplitude signals, which have inherently poor time resolution, from contributing to the time-difference distributions.

This discrepancy between the distributions in Fig. 3 implies that the walk-correction using the  $^{60}\text{Co}$  source results in an induced dynode-amplitude dependent timing artifact for the experimental data during the LaBr $_3$ (Ce) walk-correction process. Though this effect would not impact the method presented in the next section, the  $\sim\!100$  ps degradation of the time resolution would limit the ability to carry out level-lifetime measurements at very short times. It is for this reason that a second order correction is applied to the dynode amplitude for the experimental data.

Fig. 4a shows the two-dimensional dynode signal amplitude vs. time difference for all data collected during the experiment. The coincident  $LaBr_3(Ce)$  detector energies were restricted to >30 keV and <1400 keV to be in the range of the  $LaBr_3(Ce)$  walk correction. Fig. 4b provides the centroid position, extracted from the projection fits, for each dynode amplitude bin in Fig. 4a. These centroid values are then fit with a high-order polynomial, displayed as a red line in Fig. 4b, to extract the second order timing correction at each dynode signal amplitude.

The result of the second order dynode timing correction is given in Figs. 4c and 4d. Fig. 4c shows the corrected two-dimensional dynode amplitude vs. dynode, LaBr<sub>3</sub>(Ce) walk-corrected, and second order corrected dynode time difference spectrum for the experimental data.

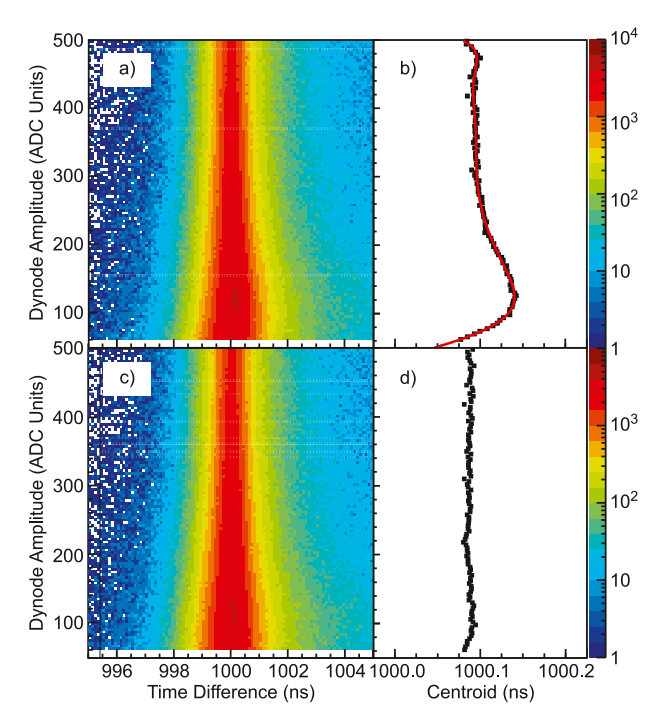


Fig. 4. (a) Two-dimensional histogram of the dynode signal amplitude plotted against the LaBr<sub>3</sub>(Ce) - PSMPT dynode time difference for a single LaBr<sub>3</sub>(Ce) detector gated on >30 keV and <1400 keV in that detector so as to be in the range of the LaBr<sub>3</sub>(Ce) walk correction. (b) Plot of centroid position, extracted from fitting the projection of each bin in (a) onto the time-difference axis. A high order polynomial, shown in red, was used for interpolation between the data to extract the time walk as a function of dynode signal amplitude. (c) Two-dimensional histogram of the dynode signal amplitude plotted against the LaBr<sub>3</sub>(Ce) - PSMPT dynode time difference for a single LaBr<sub>3</sub>(Ce) detector gated on >30 keV and <1400 keV in that detector after applying the second-order dynode timing correction. (d) Plot of centroid position, extracted from fitting the projection of each bin in (c) onto the time-difference axis.

Fig. 4d displays the dynode, LaBr<sub>3</sub>(Ce) walk-corrected, and second order corrected dynode time-difference centroid values for each bin of Fig. 4c. The high time difference tail apparent in Figs. 4a and 4c (note higher intensities on high-time side of distribution compared to the low-time side) are from the excited state lifetimes present throughout the data. The resulting centroid values are all within 30 ps of a constant offset of  $\sim 1000.1$  ns across the entire dynode dynamic range.

With the walk correction process complete, attention is focused on accounting for the difference in plastic scintillator time resolution between the source data and the experimental data due to differences in the energy distributions of radiation and DOI effects. The lifetime extraction technique presented later in this section utilizes the <sup>60</sup>Co source data to model the detector response. Therefore, we require an understanding of the difference in detector responses between an external source and an internally deposited activity. In general, the DOI effects are studied heavily in the medical imaging community, and have been shown to have the potential to alter time resolutions significantly [20].

To quantify the effect on timing resolution in the present system, the decay of the 1077.4 keV state in  $^{68}$ Zn was studied. Populated by the  $\beta$  decay of  $^{68}$ Cu, this level in  $^{68}$ Zn decays to the ground state with a half life of 1.61 ps [25]. The half life is below the sensitivity of  $\beta\gamma$  timing methods as implemented with the detectors in this experimental setup and, therefore, it is considered to be prompt from hereon forward.

The LaBr<sub>3</sub>(Ce) energy spectrum for all ten detectors, gated on dynode amplitudes of >60 and <500 ADC units, in the region around 1077.4 keV is found in Fig. 5. The peak and background regions used

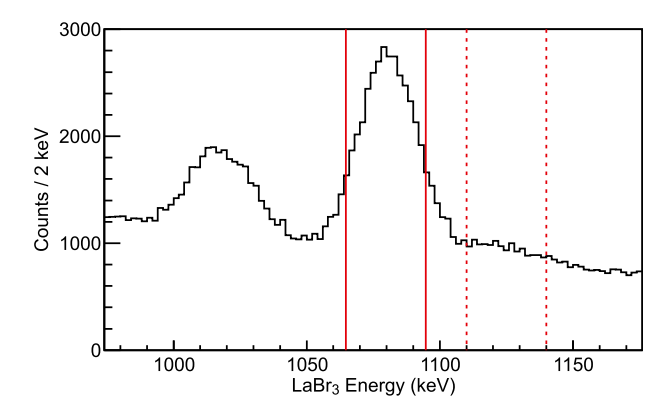
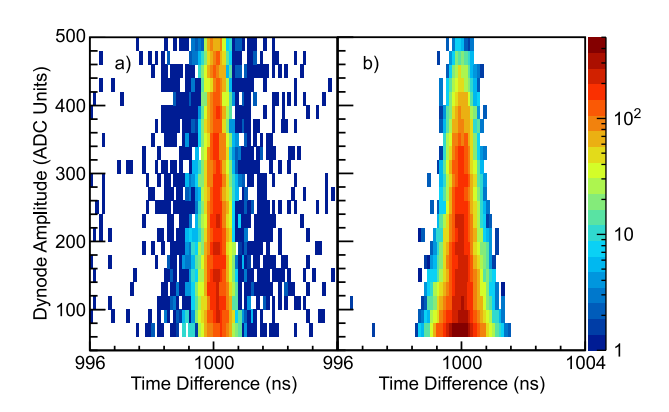


Fig. 5. (a) LaBr<sub>3</sub>(Ce) energy spectrum for all ten detectors, gated on dynode amplitudes of >60 and <500 ADC units, in the region around 1077.4 keV. The peak and background regions used for this analysis are denoted with red solid and dashed lines, respectively.



**Fig. 6.** (a) Background-subtracted 2D dynode signal amplitude vs. time difference spectrum for the 1077.4-keV peak in the experimental data. (b) The 2D dynode signal amplitude vs. time difference spectrum for the <sup>60</sup>Co source measurements for the same energy gate as (a).

for this analysis are denoted with red solid and dashed lines, respectively. The peak region is from 1064–1094 keV while the background covers the 1110–1140 keV range.

The peak and background regions were used to gate the 2D dynode signal amplitude vs. time difference spectrum for both the experimental and source data. In the case of the experimental data, the background-gated 2D spectrum was scaled to match the background counts in the peak region, and subtracted from the 2D spectrum in the peak region. This removes any response from potentially non-prompt contributions from Compton scattering of higher energy transitions. The background-subtracted 2D dynode signal amplitude vs. time difference spectrum for the experimental data in the peak region of Fig. 5 is presented in Fig. 6a. The 2D spectrum for the source data over the same LaBr<sub>3</sub>(Ce) energy region as Fig. 6a is given in Fig. 6b.

The time resolution as a function of dynode signal amplitude was determined for both the experimental and source data by projecting each bin of the 2D spectra shown in Figs. 6a and 6b, respectively, onto the time difference axis and fitting a Gaussian function to each projection. The Gaussian distribution standard deviation,  $\sigma$ , values (in ns) obtained from these projection fits are displayed as a function of dynode signal amplitude in Fig. 7a. The data for the experimental time response are the blue circles while the source results are the black squares. Each of the two response curves are fit with a power law, which was the best fit from a chi-square minimization analysis, and which is drawn in its respective color in Fig. 7a.

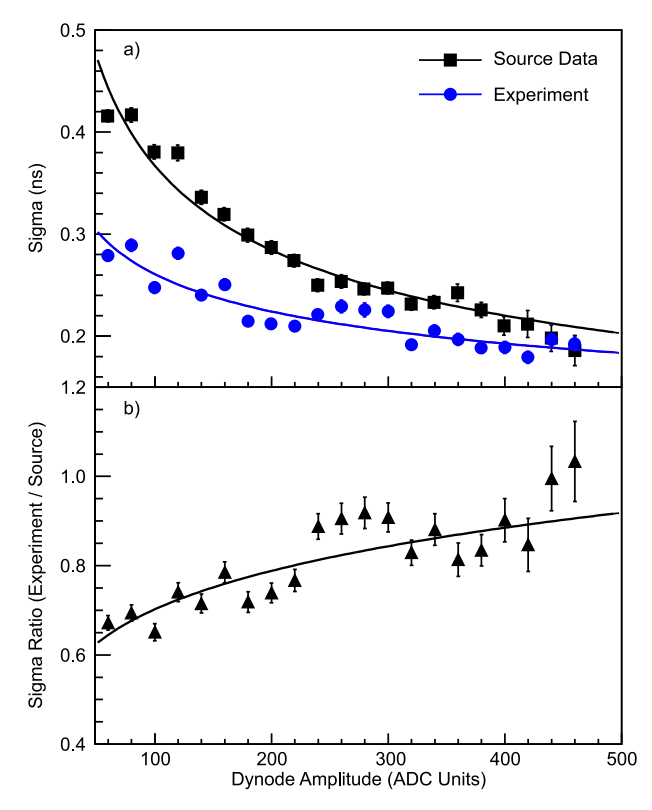


Fig. 7. (a) Sigma, in ns, as a function of dynode signal amplitude shown in blue circles for the experimental data and as black squares for the source data presented in Figs. 6a and 6b, respectively. (b) The ratio (experiment/source) of sigma values from (a) as a function of dynode signal amplitude. The fit to the data represents the correction for the time resolution (see text for details).

Fig. 7b shows the ratio of the experimental data to the source ones as a function of dynode signal amplitude. The distribution of ratios is fit with a power law which is drawn as a solid black line in 7b. The fit to the ratios represents the dynode amplitude-dependent correction factor that must multiply the sigma value for the source data in the method described in the next subsection.

#### 5.3. New analysis method for $\beta \gamma$ lifetime techniques

As seen in the previous sections, the use of a thick plastic scintillator introduces a host of features into the analysis for  $\beta \gamma$  lifetime measurements. The amplitude dependence of the plastic scintillator response removes the ability to accurately fit the data with the convolution of a single Gaussian response and an exponential decay curve. If one tries to do this, it becomes immediately obvious that a single Gaussian distribution is unable to fit the data properly. An example of this behavior is illustrated in Fig. 8 for the 478-keV,  $0_3^+ \rightarrow 2_1^+$  transition in <sup>68</sup>Ni, where using a single Gaussian fit leads to a skewing of the results that is caused by not accounting for variations in the detector response. The net effect is to skew the extracted half-life to a value that is systematically too small, as the counts that should be present in a convolution that properly describes the detector response are now attributed as shorter times in the half-life distribution. Thus, the convolution of a continuum of Gaussian response functions with an exponential decay weighted by the number of counts at each energy in the continuum must be employed. In reality, the continuous distributions are discretized into bins and the technique to describe the detector system time response,

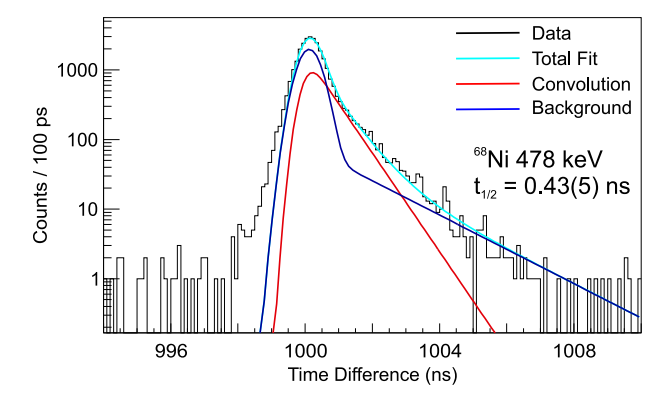


Fig. 8. Results of fitting the LaBr $_3$ (Ce) - PSPMT dynode time differences for the 2511 keV state in  $^{68}$ Ni using a single Gaussian distribution representing the detector time response in the convolution of the Gaussian response and an exponential decay curve. The total time difference spectra for the selected LaBr $_3$ (Ce) energy and scaled detector response are shown in black and blue, respectively. The total fit of the detector response for the counts under the peak is given in red, and the total fit including the background data is given in cyan.

 $R(t, t_0, \tau, E_p, E_{\gamma})$ , can be summarized by Eq. (5.1);

$$\begin{split} R(t,t_0,\tau,E_p,E_{\gamma}) &= sB(t) + \sum_{i=1}^n \sum_{E_p=E_0}^{E_F} \\ L_{i,E_p,E_{\gamma}} P_{E_p,E_{\gamma}} [f(t,t_0,i,E_p,E_{\gamma}) \otimes g(t,t_0,\tau)] \end{split}$$
 with:

$$f(t,t_0,i,E_p,E_\gamma) = \mathrm{Exp} \left[ -\frac{1}{2} \left( \frac{(t-t_0)}{D(E_p) \sigma_i(E_p,E_\gamma)} \right)^2 \right]$$

$$g(t,t_0,\tau) = \operatorname{Exp}\left[-\frac{(t-t_0)}{\tau}\right]$$

In Eq. (5.1), B(t) represents the background underneath the peak. Typically, B(t) is sampled from nearby regions with minimal spectral interference. If a peak sits on a Compton edge, a more rigorous determination is required and is beyond the scope of this paper. In most cases, we assume the B(t) time distribution varies slowly as a function of energy so it can be approximated by the distribution from above the peak of interest and the background scale factor, s, is close to one.

The Gaussian response function,  $f(t,t_0,i,E_p,E_\gamma)$ , is characterized by a centroid,  $t_0$ , and a time response width,  $\sigma_i(E_p,E_\gamma)$ . The value of  $\sigma_i(E_p,E_\gamma)$  for a given LaBr<sub>3</sub>(Ce) detector, i, in a total of n detectors, depends on the photopeak energy,  $E_\gamma$ , and the plastic scintillator energy,  $E_p$  which has to be determined for each lifetime measurement and is defined by a lower boundary  $(E_0)$  and upper boundary  $(E_F)$ . The DOI correction, which also embeds corrections related to differences between the emitted radiation energy distribution between the source calibration data and the experimental data (Section 5.2), is represented by  $D(E_p)$ . The walk corrections presented above have removed the energy and detector dependencies from  $t_0$ .

The exponential decay of the excited state  $g(t,t_0,\tau)$  depends only on the centroid,  $t_0$ , and the mean lifetime,  $\tau$ , of the decaying state. In Eq. (5.1),  $g(t,t_0,\tau)$  is convolved with the detector response,  $f(t,t_0,i,E_p,E_\gamma)$ , for each LaBr<sub>3</sub>(Ce) detector, i, and plastic scintillator dynode amplitude,  $E_p$ , at a specific photopeak energy  $E_\gamma$ . The resulting convolution is scaled by the relative contribution of each LaBr<sub>3</sub>(Ce) detector, denoted as  $L_{i,E_p,E_\gamma}$ , and the dynode amplitude distribution,  $P_{E_p,E_\gamma}$ , to derive the total convolution.

The linear combination of convolution functions describes the shape of the time distribution for the decay of a particular state of interest. That distribution function is sampled many times using Monte Carlo methods, and the results are histogrammed. The resulting histogram

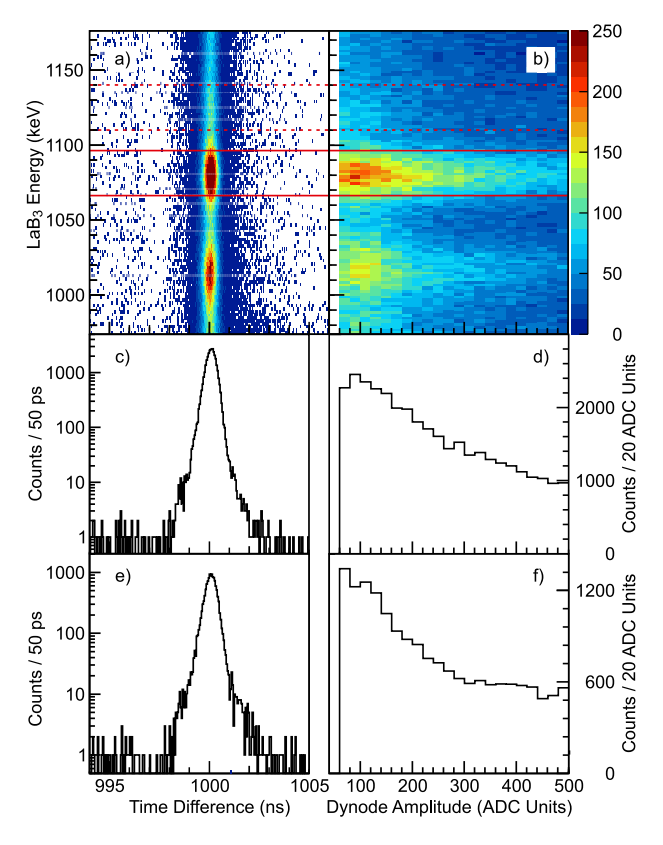


Fig. 9. (a) LaBr $_3$ (Ce) energy vs. time difference and (b) LaBr $_3$ (Ce) energy vs. dynode amplitude, respectively, for the same LaBr $_3$ (Ce) energy range as in Fig. 5. The same 1064–1094 keV peak and 1110–1140 keV background regions illustrated in Fig. 5 are shown again by red solid and dashed lines, respectively. Panels (c) and (d) show the projections of panels (a) and (b) onto the time-difference and dynode amplitude axes, respectively, for the peak region between the solid red lines. Panels (e) and (f) show the projections of panels (a) and (b) onto the time-difference and dynode amplitude axes respectively, for the background region between the dashed red lines.

is scaled to the number of counts in the peak over the region of interest, added to the scaled background, sB(t), and compared with the experimental data. A chi-square minimization is performed using many trial lifetimes, and a result is obtained from the fit of a chi-square distribution

Throughout the remainder of this section, the validity of the technique will be demonstrated on three different excited states, all with known lifetimes. The first of these states is the 1077.4-keV state in <sup>68</sup>Zn, which was used to obtain the timing resolution correction. This is a simple case because, with a prompt decay, there is no convolution and only the energy-dependent Gaussian detector response remains. In particular, this test probes our ability to reproduce the time spectrum with no free parameters.

Figs. 9a and 9b present the LaBr<sub>3</sub>(Ce) energy vs. time difference and vs. dynode amplitude, respectively, for the same LaBr<sub>3</sub>(Ce) energy range as in Fig. 5. The same 1064–1094 keV peak and 1110–1140 keV background regions illustrated in Fig. 5 are used here as well and are once again depicted by red solid and dashed lines, respectively.

Figs. 9c and 9e are the projections of Fig. 9a onto the time-difference axis for the peak and background regions, respectively. Fig. 9c represents the total time difference spectrum we strive to reproduce while Fig. 9e is the unscaled background, which is B(t) from Eq. (5.1). The scale factor, s, is obtained by fitting the 1D LaBr<sub>3</sub>(Ce) energy spectrum and comparing the total number of counts in both the peak and in the background regions over the region of interest to the integrated counts in the peak, giving a value for s > 1. For this case, s = 1.05.

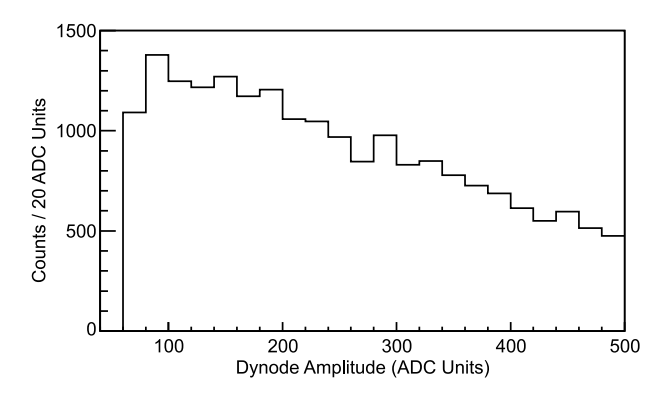


**Fig. 10.** Dynode signal amplitude distribution for the LaBr<sub>3</sub>(Ce) - dynode coincidence events between 1064 and 1094 keV. This distribution is obtained by subtracting the data in Fig. 9f, scaled by s, from Fig. 9d. The counts at each dynode energy,  $E_p$  at this specific  $\gamma$  energy,  $E_\gamma$  is  $P_{E_p,E_p}$  from Eq. (5.1).

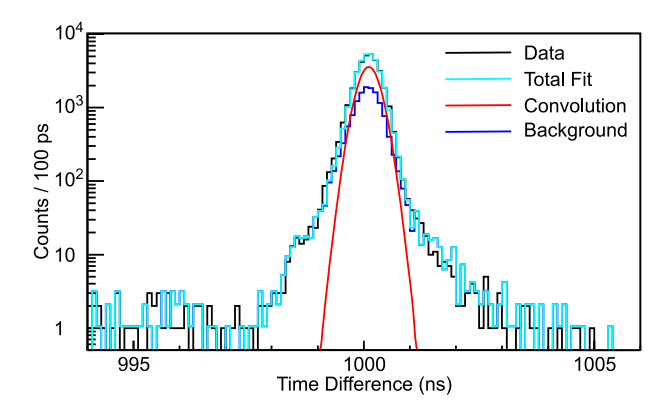


Fig. 11. Results of the fitting technique for the 1077.4-keV state in  $^{68}$ Zn. The total time difference spectrum for the 1064–1094 keV LaBr<sub>3</sub>(Ce) energy region, also shown in Fig. 9c, is in black. The scaled background time-difference spectrum over the 1110–1140 keV LaBr<sub>3</sub>(Ce) energy region is in blue, while the total fit of the detector response for the counts under the peak is in red and the total fit is in cyan.

Figs. 9d and 9f are the projections of Fig. 9b onto the dynode signal amplitude axis for the peak and background regions, respectively. The data in Fig. 9f, scaled appropriately, are subtracted from the data in Fig. 9d to yield the final dynode amplitude distribution, shown in Fig. 10, for the counts under the peak in the region of interest and, thus, is  $P_{E_0,E_n}$  from Eq. (5.1).

The values of  $L_{i,E_p,E_\gamma}$  are obtained from the individual LaBr<sub>3</sub>(Ce)  $\beta\gamma$  coincidence spectra. The counts for each detector for the background energy region, scaled by s, are subtracted from the counts of each respective detector in the peak energy region.

Sigma values,  $\sigma_l(E_p, E_\gamma)$ , are obtained from the  $^{60}$ Co source data as a function of dynode signal amplitude,  $E_p$  for the specific LaBr<sub>3</sub>(Ce) energy region,  $E_\gamma$  with the same method described above to obtain the plots shown in Fig. 7a. The DOI correction,  $D(E_p)$ , of Fig. 7b is then applied.

All quantities needed to fit the data have been extracted and the results of the procedure for the 1077.4-keV state in <sup>68</sup>Zn are presented in Fig. 11. In Fig. 11 the total time difference spectrum for the 1064–1094 keV LaBr<sub>3</sub>(Ce) energy region is shown in black. This is the same spectrum that is shown in Fig. 9c. The scaled background time-difference spectrum over the 1110–1140 keV LaBr<sub>3</sub>(Ce) energy region is shown in blue. The total fit of the detector response for the counts under the peak is presented in red and the total fit in cyan.

This test demonstrates the ability to completely describe the time response of the detector system. The stochastic background is accounted

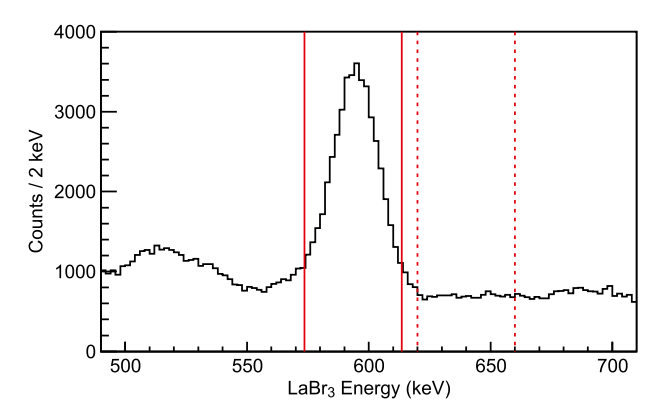


Fig. 12. (a) LaBr<sub>3</sub>(Ce) energy spectrum for all ten detectors, gated on dynode amplitudes of >60 and <500 ADC units, in the region around 594.3 keV. The peak and background regions used for the analysis are denoted with red solid and dashed lines, respectively.

for by the scaled background contribution, and the method takes into account the various higher order amplitude-dependent detector response effects to reproduce the experimental spectrum to a high degree. A value of 162 was obtained for the total chi-square for this fit in the range of 998–1002 ns time difference.

With the technique demonstrated for a prompt transition, we now focus on measuring two excited states with known lifetimes. The first of these is the 915.3-keV state in  $^{69}$ Ni. This level has a previously measured half life of 120(34) ps, and there is strong direct feeding from the  $\beta$  decay of  $^{69}$ Co [26]. The state is depopulated exclusively by a 594.3-keV  $\gamma$  ray.

The LaBr<sub>3</sub>(Ce) spectrum in the region around 594.3 keV coincident with counts in the dynode between 60 and 500 ADC units is found in Fig. 12. Again the peak and background energy regions of interest are denoted with solid and dashed red lines, respectively.

The total detector response function described in Eq. (5.1) was constructed for fourteen trial half-lives and the chi-square between  $R(t,t_0,\tau,E_\gamma,E_p)$  and the experimental data was calculated for each of these. Fig. 13 displays the distribution of  $\chi^2$  values as black squares for the set of trial half lives used in the analysis, where the conversion from mean lifetime,  $\tau$ , to half-life,  $t_{1/2} = \tau \ln(2)$ , has already been performed to show the figure. A second order polynomial, presented in Eq. (5.2), was used to fit the chi-square distribution and corresponds to the solid red line in Fig. 13.

$$\chi^2 = a\tau^2 + b\tau + c \tag{5.2}$$

The fit is used to extract the mean lifetime and its uncertainty, and thereby the half life and its uncertainty, from the chi-square distribution using Eqs. (5.3) and (5.4), respectively [28];

$$\tau = -\frac{b}{2a} \tag{5.3}$$

$$\sigma_{\tau}^2 = 2 \left( \frac{\partial^2 \chi^2}{\partial \tau^2} \right)^{-1} \tag{5.4}$$

Using the parameters of the fit, as well as combining in quadrature the statistical uncertainty along with systematic uncertainties investigated by varying quantities such as the ratio of counts in the peak to counts in the background, the centroid of the underlying Gaussian component of the convolution, and the magnitude of the timing resolution correction, we obtain a value of 135(10) ps for the 915.3-keV state in <sup>69</sup>Ni. The newly measured value agrees with the previously measured one of 120(34) ps [27] and decreases the uncertainty by a factor of three. Using the value obtained from the chi-square analysis, the best-fit total convolution was constructed. Fig. 14 provides the results of the fitting process for this 915.3-keV state in <sup>69</sup>Ni.

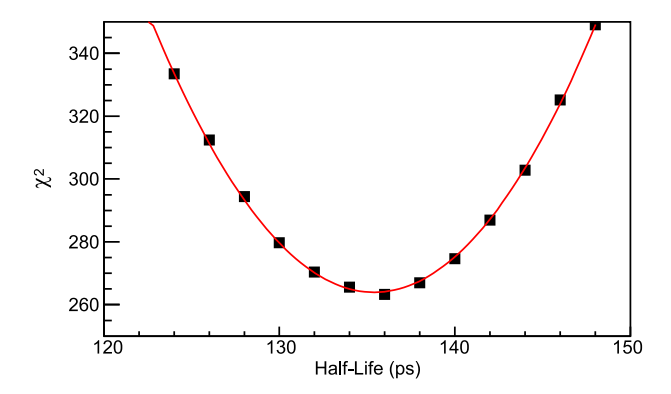


**Fig. 13.** Distribution of  $\chi^2$  values obtained by comparing the total fit,  $R(t,t_0,\tau,E_\gamma,E_p)$ , and the experimental data, shown as cyan and black in Fig. 14, respectively, for fourteen half life values equally distributed about the minimum. The conversion from mean lifetime,  $\tau$ , to half-life,  $t_{1/2} = \tau \ln(2)$ , has been performed to show the figure. The distribution is fit with a second order polynomial given in red. The location of the minimum represents the half life of the state, and the second derivative of the fit is the error on that value. We obtain a half life of 135(10) ps for the 915.3-keV state in <sup>69</sup>Ni which agrees with the previously measured 120(34) ps value [27].

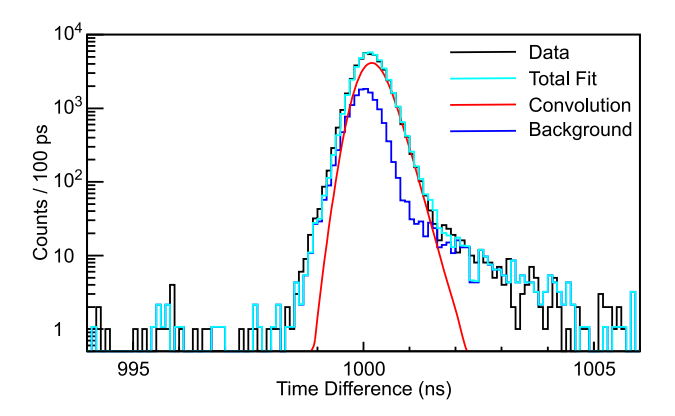


Fig. 14. Results of the fitting technique for the 915.3-keV state in  $^{69}$ Ni. The total time difference spectrum for the 574–614 keV LaBr $_3$ (Ce) energy region is in black. The scaled background time-difference spectrum over the 620–660 keV LaBr $_3$ (Ce) energy region is in blue, while the total fit of the detector response for the counts under the peak is in red and the total fit is in cyan.

The total time difference spectrum for the 574–614 keV LaBr<sub>3</sub>(Ce) energy region is in black. The scaled background time-difference spectrum over the 620–660 keV LaBr<sub>3</sub>(Ce) energy region is in blue, while the best fit convolution for the counts under the peak is in red and the resulting total best-fit to the data is in cyan. Once again, the technique reproduces all the features of the data.

The second state used to benchmark the technique is the 2677-keV level in  $^{70}$ Ni, which is depopulated exclusively by a 448.5-keV  $\gamma$  ray. This state has a previously measured half life of 1.05(3) ns [27].

The LaBr<sub>3</sub>(Ce) spectrum in the region around 448.5 keV, coincident with counts in the dynode between 60 and 500 ADC units, is found in Fig. 15. Again the peak and background energy regions of interest are denoted with solid and dashed red lines, respectively. For this region, the background must be sampled below the peak in order to avoid any contamination from the 478-keV transition in <sup>68</sup>Ni, which is the focus of a separate publication [29].

The analysis for the  $^{70}$ Ni 2677-keV state in is identical to that described for the 915.3-keV level in  $^{69}$ Ni. The resulting  $\chi^2$  distribution

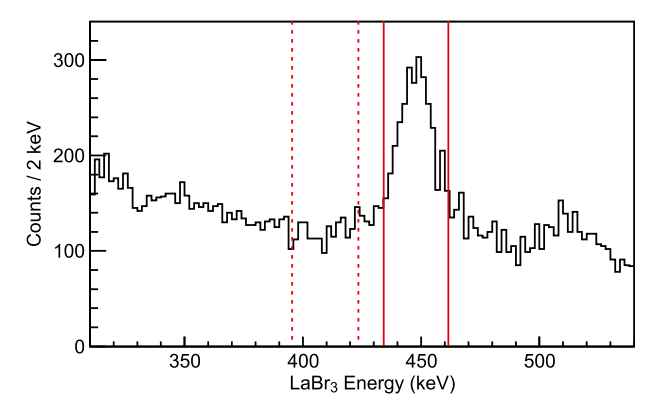
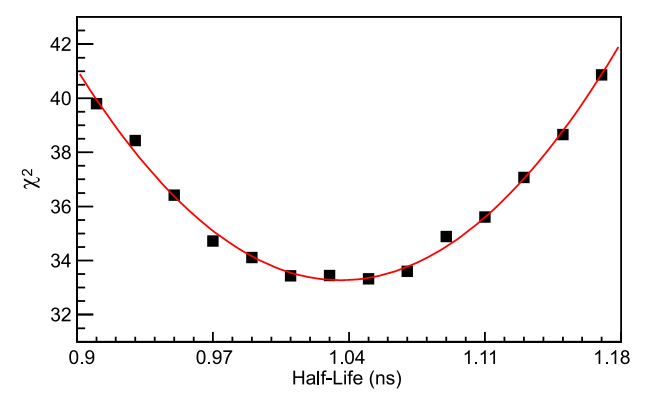


Fig. 15. (a) LaBr $_3$ (Ce) energy spectrum for all ten detectors, gated on dynode amplitudes of >60 and <500 ADC units, in the region around 448.5 keV. The peak and background regions used for the analysis are denoted with red solid and red dashed lines, respectively.



**Fig. 16.** Distribution of  $\chi^2$  values obtained by comparing the total fit and the experimental data, shown as cyan and black in Fig. 14, respectively, for fourteen half life values equally distributed about the minimum. The distribution is fit with a second order polynomial in red. The location of the minimum represents the half life of the state and the second derivative of the fit is the error on that value. We obtain a lifetime of 1.04(0.24) ns for the 2677-keV state in  $^{70}$ Ni.

for the fourteen trial half lives distributed evenly about the minimum is presented in Fig. 16. The same fitting procedure for the chi-square distribution using the Eq. (5.2) was carried out and the result corresponds to a solid red line in Fig. 16.

From the fit of the chi-square distribution, Eqs. (5.3) and (5.4), and adding statistical and systematic sources of uncertainty in quadrature, a value of 1.04(24) ns for the half life of the 2677-keV state in  $^{70}$ Ni was obtained. The relatively large error is due to low statistics, but the result agrees well with the previously measured value of 1.05(3) ns [27].

Again, with the value obtained from the chi-square analysis the, best-fit total convolution was constructed and the results of the fitting process can be found in Fig. 17.

The total time difference spectrum for the  $434-462~keV~LaBr_3(Ce)$  energy region is displayed in black. The scaled background time-difference spectrum over the  $396-424~keV~LaBr_3(Ce)$  energy region is in blue, while the best-fit convolution for the counts under the peak is in red and the resulting total best-fit to the data is in cyan. Once again, the technique is reproducing all the features of the data.

Finally, to come back full-circle to the 478-keV  $0_3^+ \rightarrow 2_1^+$  transition in <sup>68</sup>Ni using the method described in this manuscript, the results are shown in Fig. 18. As can be seen, the systematic skewing of results to shorter half-lives has been removed, and the fitted results

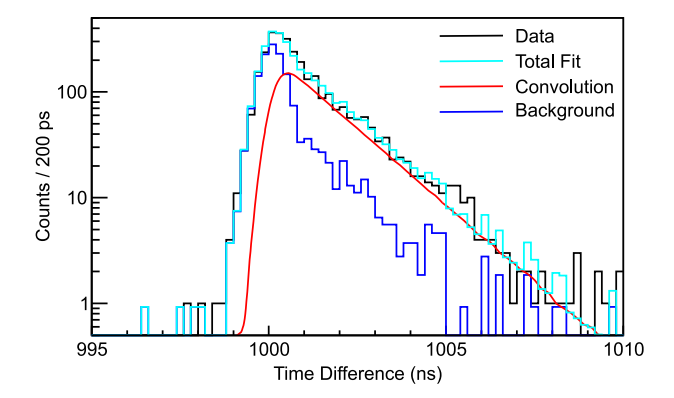


**Fig. 17.** Results of the fitting technique for the 2677-keV state in <sup>70</sup>Ni. The total time difference spectrum for the 396–424 keV LaBr<sub>3</sub>(Ce) energy region is given in black. The scaled background time-difference spectrum over the 434–462 keV LaBr<sub>3</sub>(Ce) energy region is in blue, while the total fit of the detector response for the counts under the peak is in red and the total fit is in cyan.

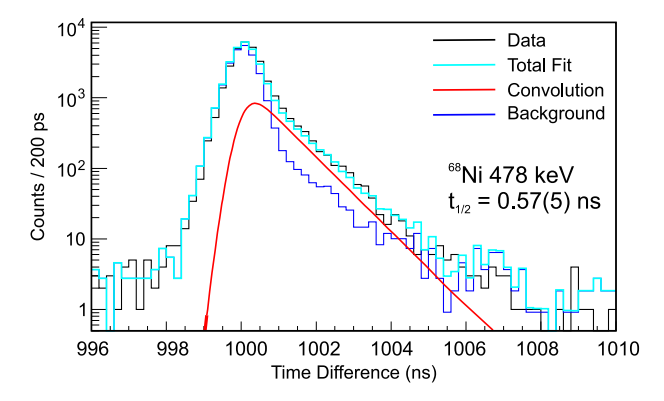


Fig. 18. Results of the fitting technique described in this manuscript for the 2511-keV state in  $^{68}$ Ni. The total time difference spectra for the selected LaBr<sub>3</sub>(Ce) energy and scaled background regions are in black and blue, respectively. The total fit of the detector response for the counts under the peak is in red and the total fit is in cyan.

more accurately represent the experimental data. This result is the one reported in Ref. [29].

## 6. Conclusions

This work has developed new methods to perform timing measurements using thick scintillators. More specifically, these methods were developed for  $\beta \gamma$  lifetime measurements, where the thick scintillator was used for ion implantation and subsequent electron detection. However, these techniques are rather general and are applicable for a variety of timing methods. We presented in detail the procedure to perform the signal-amplitude dependent time walk and timing resolution corrections necessary to characterize the detector response and facilitate the compilation of statistics from the different detectors composing the array. Then a Monte Carlo method coupled with a chisquare analysis was formulated that makes use of the measured detector responses from 60Co source data to analyze the experimental data and deduce excited state lifetimes. The method was developed in detail for the prompt 1077.4 keV transition in <sup>68</sup>Zn and was then benchmarked using two excited states, one in 69Ni and one in 70Ni, with previously measured lifetimes of 120(34) ps and 1.05(3) ns, respectively [27]. We obtained 135(10) ps and 1.04(24) ns, respectively, demonstrating the validity of the new method, and reducing the error by a factor of three for the 69Ni state.

## Declaration of competing interest

The authors declare that they have no known competing financial interests or personal relationships that could have appeared to influence the work reported in this paper.

#### Data availability

Data will be made available on request.

# Acknowledgments

The authors would like to thank J. A. Winger and T. H. Ogunbeku for fruitful discussions in the preparation of this manuscript. This work was supported in part by National Science Foundation (NSF) under Grant No. PHY 1848177 (CAREER) and contract No. PHY-1102511, by the Department of Energy National Nuclear Security Administration (NNSA) under Award No. DE-NA0000979 and Award No. DE-FG52-08NA28552, by the U.S Department of Energy, Office of Science, Office of Nuclear Physics, under contract No. DE-AC-06CH11357 (ANL) and Grant Nos. DE-FG02-94ER40834 (Maryland), DE-FG02-96ER40983 (UT), DE-FG02-97ER41041 (UNC), DE-FG02-97ER41033 (TUNL), and DE-SC-0020451 (MSU).

#### References

- [1] T. Otsuka, T. Suzuki, M. Honma, Y. Utsuno, N. Tsunoda, K. Tsukiyama, M. Hjorth-Jensen, Novel features of nuclear forces and shell evolution in exotic nuclei, Phys. Rev. Lett. 104 (2010) 012501, http://dx.doi.org/10.1103/PhysRevLett.104.012501, URL https://link.aps.org/doi/10.1103/PhysRevLett.104.012501.
- [2] J. Dobaczewski, I. Hamamoto, W. Nazarewicz, J.A. Sheikh, Nuclear shell structure at particle drip lines, Phys. Rev. Lett. 72 (1994) 981–984, http:// dx.doi.org/10.1103/PhysRevLett.72.981, URL https://link.aps.org/doi/10.1103/ PhysRevLett.72.981.
- [3] S. Pommé, The uncertainty of the half-life, Metrologia 52 (3) (2015) S51–S65, http://dx.doi.org/10.1088/0026-1394/52/3/s51.
- [4] A. Blaugrund, Notes on Doppler-shift lifetime measurements, Nucl. Phys. 88 (3) (1966) 501–512, http://dx.doi.org/10.1016/0029-5582(66)90409-3, URL http://www.sciencedirect.com/science/article/pii/0029558266904093.
- [5] D. Branford, I. Wright, A doppler shift attenuation method for measuring lifetimes in the range 10–13–10–15S using heavy-ion induced reactions, Nucl. Instrum. Methods 106 (3) (1973) 437–443, http://dx.doi.org/10.1016/0029-554X(73)90304-2, URL http://www.sciencedirect.com/science/article/pii/0029554X73903042.
- [6] S. Devons, G. Manning, D.S.P. Bunbury, Measurement of γ -transition lifetimes by recoil methods, Proc. Phys. Soc. Section A 68 (1) (1955) 18, URL http: //stacks.iop.org/0370-1298/68/i=1/a=304.
- [7] T.K. Alexander, K.W. Allen, Lifetimes of the 160 6.13-MeV level and the 170 0.871-MeV level, Can. J. Phys. 43 (9) (1965) 1563–1573, http://dx.doi.org/10. 1139/p65-148.
- [8] A. Dewald, O. Möller, P. Petko, Developing the recoil distance Doppler-shift technique towards a versatile tool for lifetime measurements of excited nuclear states, Prog. Part. Nucl. Phys. 67 (3) (2012) 786–839, http://dx.doi. org/10.1016/j.ppnp.2012.03.003, URL http://www.sciencedirect.com/science/ article/pii/S01466410120000713.
- [9] P. Bizzeti, A. Bizzeti-Sona, Integral- and differential-decay-curve methods for recoil distance measurements of nuclear lifetimes, Nucl. Instrum. Methods Phys. Res. A 736 (2014) 179–183, http://dx.doi.org/10.1016/j.nima.2013.11.017, URL http://www.sciencedirect.com/science/article/pii/S0168900213015568.
- [10] H. Mach, R. Gill, M. Moszyński, A method for picosecond lifetime measurements for neutron-rich nuclei: (1) outline of the method, Nucl. Instrum. Methods Phys. Res. A 280 (1) (1989) 49–72, http://dx.doi.org/10.1016/0168-9002(89)91272-2, URL http://www.sciencedirect.com/science/article/pii/0168900289912722.
- [11] G. Suliman, S. Pommé, M. Marouli, R.V. Ammel, V. Jobbágy, J. Paepen, H. Stroh, C. Apostolidis, K. Abbas, A. Morgenstern, Measurements of the half-life of 214Po and 218Rn using digital electronics, Appl. Radiat. Isot. 70 (9) (2012) 1907–1912, http://dx.doi.org/10.1016/j.apradiso.2012.02.095, URL http://www.sciencedirect.com/science/article/pii/S0969804312001431 Proceedings of the 18th International Conference on Radionuclide Metrology and its Applications.
- [12] M. Tatcher, H. Lindeman, Measurement of half-lives of isomeric nuclear states by a method of time interval analysis, Nucl. Instrum. Methods 61 (1) (1968) 58–60, http://dx.doi.org/10.1016/0029-554X(68)90449-7, URL http:// www.sciencedirect.com/science/article/pii/0029554X68904497.

- [13] H. Lindeman, N. Rosen, A generalization of the Marsden-Barratt law for time-correlated radioactive decay, Physica 23 (1) (1957) 436–440, http://dx.doi.org/10.1016/S0031-8914(57)92832-X, URL http://www.sciencedirect.com/science/article/pii/S003189145792832X.
- [14] M. Moszyński, H. Mach, A method for picosecond lifetime measurements for neutron-rich nuclei: (2) Timing study with scintillation counters, Nucl. Instrum. Methods Phys. Res. A 277 (23) (1989) 407–417, http://dx.doi.org/10.1016/ 0168-9002(89)90770-5, URL http://www.sciencedirect.com/science/article/pii/ 0168900289907705.
- [15] C. Prokop, S. Liddick, B. Abromeit, A. Chemey, N. Larson, S. Suchyta, J. Tompkins, Digital data acquisition system implementation at the National Superconducting Cyclotron Laboratory, Nucl. Instrum. Methods Phys. Res. A 741 (2014) 163–168, http://dx.doi.org/10.1016/j.nima.2013.12.044, URL http://www.sciencedirect.com/science/article/pii/S0168900213017488.
- [16] C. Prokop, S. Liddick, N. Larson, S. Suchyta, J. Tompkins, Optimization of the national superconducting cyclotron laboratory digital data acquisition system for use with fast scintillator detectors, Nucl. Instrum. Methods Phys. Res. A 792 (2015) 81–88, http://dx.doi.org/10.1016/j.nima.2015.04.052, URL http://www. sciencedirect.com/science/article/pii/S0168900215005550.
- [17] D. Morrissey, B. Sherrill, M. Steiner, A. Stolz, I. Wiedenhoever, Commissioning the {a1900} projectile fragment separator, Nucl. Instrum. Methods Phys. Res. B 204 (2003) 90–96, http://dx.doi.org/10.1016/S0168-583X(02)01895-5, URL http://www.sciencedirect.com/science/article/pii/S0168583X02018955 14th International Conference on Electromagnetic Isotope Separators and Techniques Related to their Applications.
- [18] M. Alshudifat, R. Grzywacz, S. Paulauskas, Development of a segmented scintillator for decay studies, Physics Procedia 66 (2015) 445–450, http://dx.doi.org/10.1016/j.phpro.2015.05.056, URL http://www.sciencedirect.com/science/article/pii/\$1875389215002096, The 23rd International Conference on the Application of Accelerators in Research and Industry {CAARI} 2014.
- [19] W. Mueller, J. Church, T. Glasmacher, D. Gutknecht, G. Hackman, P. Hansen, Z. Hu, K. Miller, P. Quirin, Thirty-two-fold segmented germanium detectors to identify -rays from intermediate-energy exotic beams, Nucl. Instrum. Methods Phys. Res. A 466 (3) (2001) 492–498, http://dx.doi.org/10.1016/S0168-9002(01)00257-1, URL http://www.sciencedirect.com/science/article/pii/S0168900201002571.
- [20] A. Ivan, K.C. Burr, Y. Shao, J.W. LeBlanc, Depth of interaction effect on timing resolution in PET block detectors, in: Nuclear Science Symposium Conference Record, 2004 IEEE, vol. 7, 2004, pp. 4156–4158, http://dx.doi.org/10.1109/ NSSMIC 2004 1466807

- [21] E. Samei, D.J. Peck, Hendee's Physics of Medical Imaging, fifth ed., Wiley-Blackwell, 2019.
- [22] A. Fallu-Labruyere, H. Tan, W. Hennig, W. Warburton, Time resolution studies using digital constant fraction discrimination, Nucl. Instrum. Methods Phys. Res. A 579 (1) (2007) 247–251, http://dx.doi.org/10. 1016/j.nima.2007.04.048, URL http://www.sciencedirect.com/science/article/pii/S0168900207006213 Proceedings of the 11th Symposium on Radiation Measurements and Applications.
- [23] E. Browne, J. Tuli, Nuclear data sheets for A=60, Nucl. Data Sheets 114 (12) (2013) 1849–2022, http://dx.doi.org/10.1016/j.nds.2013.11.002, URL http://www.sciencedirect.com/science/article/pii/S0090375213000823.
- [24] J.N. Orce, B. Crider, S. Mukhopadhyay, E. Peters, E. Elhami, M. Scheck, B. Singh, M.T. McEllistrem, S.W. Yates, Determination of the 2<sup>+</sup><sub>1</sub> → 0<sup>+</sup><sub>1</sub> transition strengths in <sup>58</sup>Ni and <sup>60</sup>Ni, Phys. Rev. C 77 (2008) 064301, http://dx.doi.org/10.1103/PhysRevC.77.064301, URL https://link.aps.org/doi/10.1103/PhysRevC.77.064301.
- [25] E. McCutchan, Nuclear data sheets for A=68, Nucl. Data Sheets 113 (67) (2012) 1735–1870, http://dx.doi.org/10.1016/j.nds.2012.06.002, URL http://www.sciencedirect.com/science/article/pii/S009037521200049X.
- [26] C. Nesaraja, Nuclear data sheets for, Nucl. Data Sheets 115 (2014) 1–134, http://dx.doi.org/10.1016/j.nds.2013.12.001, URL http://www.sciencedirect.com/science/article/pii/S0090375213000938.
- [27] H. Mach, M. Lewitowicz, M. Stanoiu, F. Becker, J. Blomqvist, M. Berge, R. Boutami, B. Cederwall, Z. Dlouhy, B. Fogelberg, L. Fraile, G. Georgiev, H. Grawe, R. Grzywacz, P. Johansson, W. Klamra, S. Lukyanov, M. Mineva, J. Mrazek, G. Neyens, F. de Oliveir Santos, M. Pfützner, Y. Penionzhkevich, E. Ramström, M. Sawicka, Coupling of valence particles/holes to 68,70Ni studied via measurements of the B(E2) strength in 67,69,70Ni and 71Cu, Nuclear Phys. A 719 (2003) C213 C216, http://dx.doi.org/10.1016/S0375-9474(03)00920-5, URL http://www.sciencedirect.com/science/article/pii/S0375947403009205.
- [28] P. Bevington, D. Robinson, Data Reduction and Error Analysis for the Physical Sciences, in: McGraw-Hill Higher Education, McGraw-Hill, 2003.
- [29] B. Crider, C. Prokop, S. Liddick, M. Al-Shudifat, A. Ayangeakaa, M. Carpenter, J. Carroll, J. Chen, C. Chiara, H. David, A. Dombos, S. Go, R. Grzywacz, J. Harker, R. Janssens, N. Larson, T. Lauritsen, R. Lewis, S. Quinn, F. Recchia, A. Spyrou, S. Suchyta, W. Walters, S. Zhu, Shape coexistence from lifetime and branching-ratio measurements in 68,70Ni, Phys. Lett. B 763 (2016) 108–113, http://dx.doi.org/10.1016/j.physletb.2016.10.020, URL http://www.sciencedirect.com/science/article/pii/S0370269316305913.